Resource limitation modulates the fate of dissimilated nitrogen in a dual-pathway Actinobacterium

David C. Vuono[a], Robert W. Read[a], James Hemp[b], Benjamin W. Sullivan[c], John A. Arnone III[a], Iva Neveux[a], Bob Blank[d], Carl Staub[e], Evan Loney[a], David Miceli[a], Mari Winkler[f], Romy Chakraborty[g], David A. Stahl[f], Joseph J. Grzymski[a,1]

[a]Division of Earth and Ecosystem Sciences, Desert Research Institute, Reno, NV 89512, USA

[b]Division of Geological and Planetary Sciences, California Institute of Technology, Pasadena, CA, USA

[c]Department of Natural Resources and Environmental Science, University of Nevada, Reno, NV 89557, USA

[d]Agricultural Research Service, U.S. Department of Agriculture, Reno, NV, 89512, USA

[e]Agtron, Inc. 9395 Double R Blvd, Reno, NV 89521, USA

[f]Department of Civil and Environmental Engineering, University of Washington, Seattle, WA, 98195, USA

[g]Lawrence Berkeley National Laboratory, Berkeley, CA, 94729, USA

[1]Correspondence: Joseph J. Grzymski, Division of Earth and Ecosystem Sciences, Desert Research Institute, Reno, 2215 Raggio Parkway, NV 89512, USA

Email: Joe.Grzymski@dri.edu

Abstract

Carbon to nitrate ($C:NO_3^-$) ratios are thought to modulate pathway selection between respiratory ammonification and denitrification, two nitrogen (N) dissimilatory processes vital to the global N budget. However, the molecular mechanisms that enable the selection of these pathways remains unclear. Here we evaluate $C:NO_3^-$ control on pathway selection in *Intrasporangium calvum* C5, a Gram-positive menaquinone-based dual-pathway denitrifier/respiratory ammonifier and show that $C:NO_3^-$ control theory is insufficient to explain pathways selection. We demonstrate that the bacterium disproportionately utilizes ammonification rather than denitrification (with nitrous oxide as its terminal end-product) when grown under carbon or nitrate limitation, not $C:NO_3^-$ ratio. The ammonification pathway also promoted higher bacterial growth rates. Time series analysis of metabolite and transcriptional profiles during growth showed that transcript abundances for nitrite reducing complexes, NrfAH and NirK, significantly increased in response to nitrite production. Although lactate was the only carbon source provided to the organism, we detected formate production during growth (~200 μM), a five-fold upregulation in formate transporters, and a simultaneous up-regulation of formate dehydrogenase used to translocate protons via a quinol-loop. These results suggest that additional reducing equivalents can be obtained from a single carbon source and used for ammonification during resource limitation. Mechanistically, pathway selection may be driven by intracellular redox potential (redox poise), which is lowered during resource limitation, thereby decreasing catalytic activity of the bc_1 complex (an upstream electron transport step needed for denitrification). Our work advances our understanding of the conditions and underlying mechanisms that select for denitrification and respiratory ammonification in environmental systems.

Significance

The mechanisms regulating electron transfer through branched anaerobic respiratory chains, such as dual-pathway nitrite reduction, have remained elusive. In this work, we tested the response of resource-limitation and -excess versus $C:NO_3^-$ ratio on denitrification versus respiratory ammonification in a dual-pathway denitrifying/respiratory ammonifier from the phylum *Actinobacteria.* We discovered that carbon and nitrate scarcity promoted a higher nitrogen flux through the respiratory ammonification pathway. Thus, control of respiratory pathway, denitrification versus respiratory ammonification, is not modulated by $C:NO_3^-$ ratio, as

49 previously thought, but rather the cell's need to maximize energy recovery when either resource
50 is in short supply. This discovery has significant relevance to a developing understanding of
51 factors controlling retention or release of reactive nitrogen from environmental systems.

52 **Introduction**

53 Globally, respiratory ammonification and denitrification are vital nitrogen (N) dissimilation
54 pathways that either retain reactive N to support net primary productivity or close the N-cycle
55 through the release of N_2, respectively. The environmental controls on these two pathways have
56 gained attention due to increased anthropogenic N inputs into the environment (1). Several
57 environmental controls have been posited, particularly the ratio of electron-donor to electron-
58 acceptor (e.g., C:NO_3^-) (2), but have received limited experimental and systematic validation (3,
59 4). Furthermore, the underlying molecular mechanisms for pathway selection are still unknown.
60 Over geologic time, strong selective pressures from Earth's shifting biogeochemistry and
61 oxidation-state have driven evolutionary adaptions to microbial electron transport chains (ETC)
62 (5, 6), respiratory chain redox potentials (7–9), and protein atomic composition (10, 11), which
63 also shed light on how these pathways are regulated in contemporary organisms. Here, by
64 identifying the biochemical and evolutionary differences between respiratory ammonification
65 and denitrification, we disentangle the functional significance and molecular mechanisms of
66 electron transfer through either pathway in a dual pathway organism.

67 From a biochemical standpoint, the primary difference between respiratory ammonification and
68 denitrification is their respective source of reducing equivalents in the ETC: 1) heme-based
69 cytochrome c nitrite reductase used in respiratory ammonification receive electrons directly from
70 the quinone (Q) pool (12) while 2) copper-containing and cytochrome cd_1 nitrite reductases used
71 in denitrification receive electrons from a soluble electron carrier (e.g., cytochrome c) via the bc_1
72 complex (13). From an evolutionary standpoint, we can place each N-module's origin to a
73 putative time in Earth history based on the metal co-factors that would have been bioavailable:
74 heme-based cytochromes in an ancient, more reduced, environment compared to the copper-
75 containing nitrite reductases in an oxidizing environment (14). The bioenergetic chains of
76 microorganisms also underwent selective pressure to shift from low-potential (LP) to high-
77 potential (HP) quinones in response to Earth's oxygenation (7, 8). Menaquinone (MK) is thought
78 to be the ancestral type of LP quinone (15) typically having a redox midpoint potential ~150 mV

79 lower than the evolutionarily more recent ubiquinone (UQ) (8). Organisms that use UQ are
80 thought to have evolved under high O_2 tensions and the only clades within the bacterial domain
81 to use UQ are the *α*-, *β*-, *γ*-proteobacteria (8). Surprisingly, our understanding for the
82 biochemistry of denitrification is based predominantly on HP UQ-based systems (16), leaving a
83 significant knowledge gap in the physiology and biochemistry of LP MK-based denitrifiers and
84 how they link electron transfer with energy capture under resource limitation.

85 Dual-pathway respiratory nitrite reducers, where respiratory ammonification and denitrification
86 modules are encoded in the same genome, provide a unique system to investigate the molecular
87 mechanisms of $C:NO_3^-$ control on pathway selection as they blend the presumptively ancient
88 (NrfA) and modern (NirK) N-reducing modules. While many dual-pathway denitrifiers and
89 respiratory ammonifiers have been identified (many of which use LP ETCs), most still lack
90 phenotypic characterization (17–19). Only *Shewanella loihica* PV-4, a Gram-negative, *γ*-
91 proteobacterium that uses UQ and dimethylmenaquinone (DMK)-based bioenergetics has been
92 thoroughly characterized (3, 20, 21). Nonetheless, these dual-pathway nitrite reducers are
93 capable of differential energy conservation through pathway bifurcation of nitrite. Yet no
94 mechanistic or metabolic models exist to explain how these dual-pathway organisms partition
95 electron flow and proton translocation between pathways to maximize resource-use efficiency. It
96 is not known if these organisms differentially distribute electron flow through alternative
97 respiratory chains in response to shifting resource availability or control each pathway
98 independently in response to resource thresholds. Is there an evolutionary and biochemical basis
99 for pathway selection?

100 It has long been postulated that $C:NO_3^-$ ratio modulates the activity of respiratory
101 ammonification versus denitrification (2), with numerous studies in recent years differing in the
102 methods used to calculate $C:NO_3^-$ ratio, carbon sources used, range of C:N ratios tested,
103 magnitudes of C and N concentrations, sample types (enrichment cultures vs isolates), and
104 culturing mode (chemostat/batch culture) (Table S1) (3, 4, 22–24). The hypothesis for $C:NO_3^-$
105 control states that high $C:NO_3^-$ ratios (stoichiometric limitation of nitrate relative to C) drive
106 respiratory ammonification while low $C:NO_3^-$ ratios (stoichiometric limitation of C relative to
107 nitrate) drive denitrification. This hypothesis is based on the rationale that denitrification
108 theoretically yields more free energy per electron, but respiratory ammonification yields more

free energy per nitrate due to the stoichiometry of each reaction: one nitrate is needed to make ammonium while two are needed to make N_2O/N_2 (2, 25). Thus, when $C:NO_3^-$ ratio is low, cells select denitrification to maximize the free energy advantage per electron. When $C:NO_3^-$ is high, cells select respiratory ammonification to maximize the free energy advantage per nitrate. However, the theoretical basis for this prediction is inconsistent with the observation that growth yields of pure denitrifiers are significantly lower than expected and lower than growth yields of respiratory ammonification (25). This observation suggests that despite a lower free energy yield (ΔG) compared to denitrification, respiratory ammonification conserves more energy during catabolism, through the generation of a proton motive force (Δp) in the ETC, to build more biomass during anabolism. Thus, there is a need to better understand the effects of different resource limitations on growth and pathway selection (i.e., allocation of C and N to dissimilatory and assimilatory processes), which are often confounded by $C:NO_3^-$. For example, reportedly "low" $C:NO_3^-$ ratios rarely fall below 1.5 have rarely been tested (Table S1), conditions in which C would be a growth-limiting resource. Instead, pathway selection should be better predicted by 1) Liebig's law of the minimum (LM) and 2) the maximum power principle (MPP) (26). Under the MPP, which states that biological systems are designed to maximize power intake and energy transformation, the cell's aim is therefore to maximize power (i.e., realized in the form of growth rate and yield) given the constraints of a growth-limiting resource (i.e., LM). Therefore, limitation of a growth-limiting resource, whether it be C or NO_3^-, should dictate the selection of the most efficient respiratory module to maximize power (i.e., MPP).

If indeed there is regulatory control by $C:NO_3^-$ ratio, the predicted end-products should also remain identical at different substrate concentrations of the same ratio. In order to resolve the inconsistencies and molecular mechanisms of $C:NO_3^-$ control on pathway selection and better understand branched respiratory chains in LP-based nitrate-reducing organisms, we undertook the characterization of the novel Gram-positive actinobacterium strain *Intrasporangium calvum* C5: a dual-pathway nitrite reducer that uses MK as sole pool quinone. Physiological and genomic analysis revealed that the bacterium is a close relative to type species *I. calvum* 7KIP, reduces nitrate and nitrite using a range of carbohydrates, and uses ammonium as its sole assimilatory N source. *I. calvum*'s dissimilatory N modules are composed of a membrane-bound nitrate reductase (NarG), a copper nitrite reductase (NirK), a nitric oxide (NO) reductase (qNor), and a cytochrome c nitrite reductase (CxxCH 1st heme motif variety) with a *nrfAH* operon

140 organization. Here we show that over a range of C:NO_3^- ratios, duplicated at two substrate
141 concentrations, *I. calvum* disproportionately utilizes its ammonia-forming pathway during C
142 limitation (≤ 0.4mM lactate), when C:NO_3^- ratios are < 1 (an observation contrary to the current
143 paradigm). Using a genome-guided approach coupled to time-series transcriptomics and
144 metabolite profiles, we identified differentially expressed genes in the bacterium's ETC and
145 central metabolic pathways. Using this information to inform a metabolic reconstruction of the
146 ETC we infer mechanisms by which these two pathways are regulated at the biochemical level.

147 **Results**

148 **Genomic analysis of *I. calvum* C5.** *I. calvum* C5 was isolated from a nitrate contaminated well
149 (>200mM nitrate) at the Oak Ridge National Laboratory Field Research Station in Oak Ridge,
150 TN. The strain was selected for further analysis due to its nitrate reducing phenotype in minimal
151 media. We sequenced and analyzed the genome of *I. calvum* C5 to first compare its similarity to
152 the type species *I. calvum* 7KIP. We identified a high degree of sequence similarity to 7KIP
153 based on three homologous sequence regions as locally collinear blocks. Genome size of C5 was
154 4,025,044 base pairs (bp), only 662 bp longer than 7KIP. Genomic analysis of the ETC revealed
155 the typical suite of complexes common to facultative aerobes, including primary dehydrogenases
156 (*nuo* complex, succinate dehydrogenase), alternative *NDH-2* NADH dehydrogenase, cytochrome
157 bc_1 complex, high-oxygen adapted cytochrome c oxidase (A-family), and low-oxygen adapted
158 cytochrome *bd* oxidase. The bc_1 complex subunits are also located immediately upstream of
159 cytochrome c oxidase, suggesting that these enzymes are encoded in a single operon creating a
160 supercomplex. Despite *I. calvum*'s seeming propensity for aerobic growth on a number of
161 growth media (27), its bioenergetic system uses MK as its sole pool quinone. *I. calvum* also
162 possesses multiple pathways for supplying electrons into the MK-pool, such as formate, malate,
163 hydroxybutyrate, and glycerophosphate dehydrogenases. Once in the MK-pool, there are
164 alternative pathways for MKH_2 oxidation that can circumvent the bc_1 complex, such as a
165 membrane-bound respiratory nitrate reductase module (NarG). In addition, to NarG, its
166 dissimilatory N module composition consists of a truncated denitrification pathway (N_2O is a
167 terminal product) using a copper nitrite reductase NirK and quinol-dependent nitric oxide
168 reductase qNor. The NirK peptide sequence length in *I. calvum* is significantly longer than that
169 of canonical NirKs: 909 versus 300-500 amino acids long and has 13 predicted transmembrane

170 regions on its N-terminus. *I. calvum* also possesses both catalytic and membrane anchor subunits
171 (NrfA and NrfH, respectively) for a pentaheme cytochrome c module involved in respiratory
172 nitrite ammonification.

173 ***I. calvum* encodes for a functional NrfAH complex and assimilates NH_4^+ via respiratory**
174 **nitrite ammonification.** To gain insight into possible function of the NrfAH complex, we
175 aligned the NrfA protein sequences from C5 and 7KIP to a collection of 33 recognized
176 cytochrome c nitrite reductases from published annotated genomes (Table S2). This phylogenetic
177 analysis confirmed that NrfA from *I. calvum* is a member of the CxxCH 1st heme motif group
178 (Fig.1A), which forms one of four clades on the NrfA phylogenetic tree. The other three clades
179 consisted of taxa possessing the common CxxCK 1st heme motif. We then queried the genomes
180 of the taxa in our phylogeny for other annotated N-reducing modules used in nitrate reduction,
181 nitrite reduction, NO-forming nitrite reduction, and primary pool quinone. Among the three
182 major clades of NrfA, at least 5 additional taxa are noted having dissimilatory N-module
183 inventories containing dual respiratory pathways: *Symbiobacterium thermophilum, Bacillus*
184 *azotoformans, Bacillus bataviensis*, *Bdellovibrio bacteriovorus*, and *Candidatus* Nitrospira
185 inopinata, (Fig.1A). Also, none of the taxa in our NrfA phylogeny harbored the cd_1 nitrite
186 reductases (NirS). Due to the exclusive presence of NirK representation in dual-pathway
187 membership, we asked whether there might be differences in protein atomic composition
188 between NirK and NrfA, given the disparate evolutionary origins of these modules (28). We
189 collected 20 additional publicly available NirK protein sequences from nondual-pathway
190 denitrifiers (Table S2) and calculated the protein C and N composition for our NirK/NrfA
191 collection as atoms per residue side-chain (Fig. 1B). These results showed a significant depletion
192 in C and N per residue side-chain for NirK compared to NrfA (C and N: $p<0.001$; t-test),
193 indicating that resource constraints are imprinted on the evolution of these proteins.

194 We next tested the functionality of *I. calvum*'s Nrf complex by growing the bacterium under
195 reducing conditions using Hungate-technique prepared minimal media with reducing agent (1
196 mM cysteine) to ensure no C was consumed with residual O_2 (8 mM lactate, 12 mM nitrate,
197 ammonium-replete). We then performed a state-transition where biomass from late-exponential
198 growth phase was collected and inoculated into ammonia-deplete media (Fig. 1C). Despite no
199 detectable amounts of ammonium produced in the media over time, cell counts increased

200 $5.4x10^5 \pm 8.9x10^4$ cells/mL (0.126±0.02 optical absorbance units, OD_{600}) over a 48-hour
201 incubation, indicating consumption of ammonium produced by NrfA. Net ammonium production
202 was 13±2.7 µmoles with the remainder of dissimilated N being used by the denitrification
203 pathway (24±4.2 µmoles N_2O-N), resulting in a recovery of 97.4% dissimilated N. These results
204 confirmed that *I. calvum* C5 has a functional Nrf complex and also consumes the product
205 (ammonium) of respiratory nitrite ammonification.

206 **Respiratory nitrite ammonification exceeds denitrification under C-limitation.** We
207 investigated C:NO_3^- control on respiratory ammonification versus denitrification on cultures of *I.*
208 *calvum* C5 over a high resource C:NO_3^- range (16-0.4 mM lactate, 12 mM nitrate; ratio 4-0.1)
209 and low resource C:NO_3^- range (1.6-0.04 mM lactate, 1.2 mM nitrate; ratio 4-0.1). This
210 experimental design enabled us to evaluate C:NO_3^- control over a broader range than previous
211 studies that only considered ratios ≥ 1.5 (3, 4, 22), while also testing the effects of resource
212 concentration on pathway selection. Under all the treatments tested, gas and ion chromatography
213 measurements showed products of both respiratory pathways, differing only in the relative
214 fraction of N_2O versus ammonium production across treatments (Fig. 2). At high resource
215 concentrations, respiratory ammonification did not prevail at high C:NO_3^- ratios (Fig. 2A & 2B,
216 left panels; Table S3). Instead, significantly greater amounts of N_2O were produced over
217 ammonium, though nitrite was still the major extracellular end-product of nitrate respiration.
218 Despite the predominance of N_2O production under the high resource concentrations, ammonium
219 production exceeded N_2O production only at the lowest C:NO_3^- ratio (0.4 mM lactate, ratio=0.1)
220 (Table S3) and accounted for 76.2±0.1% of dissimilated N.

221 Results from the low resource dataset provided weak support for the strict stoichiometry
222 hypothesis that C:NO_3^- controls pathway selection. Ammonia exceeded N_2O production only
223 under one high C:NO_3^- ratio treatment (ratio=4; 1.6 mM lactate; Fig. 2AB, right panels).
224 However, at ratios ≤1 (≤0.4 mM lactate), significantly more ammonium than N_2O was produced.
225 On average, respiratory ammonification accounted for 78.1±8.9% of dissimilated N for lactate
226 concentrations ≤0.4 mM. When these results are taken in context with cell physiology, we
227 observed a significant and positive relationship between specific growth rate (μ) and the fraction
228 of N dissimilated by respiratory ammonification (R^2=0.5; p<0.001) (Fig. 2C, Fig. S1; Table S4).

229 **Resource concentration influences the metabolite profiles of ammonium and N_2O**
230 **production.** Given the co-occurrence of end products from both pathways during the end-point
231 experiments (Fig. 2), we next investigated the timing of ammonium and N_2O production relative
232 to metabolite profiles for lactate, nitrate/nitrite, and growth phase at two resource concentrations
233 with the same ratio (8 mM and 0.8 mM lactate, ratio=2; Fig. 3A, S2, respectively). Despite
234 ample e-donor and e-acceptor available for growth, the high resource cultures entered a quasi-
235 stationary phase at ~50 hours, after which there was continued slow growth (Fig. 3A).
236 Metabolite profiles showed that ammonium and N_2O production began simultaneously, as soon
237 as nitrite was produced from nitrate reduction. The low resource cultures entered stationary
238 phase at ~40 hours (Fig. S2) after nitrate had been fully utilized. No further cell growth was
239 observed after stationary phase was reached. These results show that cell growth occurs
240 primarily on the reduction of nitrate, while nitrite reduction to ammonium and N_2O takes place
241 during a stationary growth phase, demonstrating that microbial activity is not always correlated
242 with growth. The metabolite profiles for ammonium and N_2O at low resources did not mirror
243 those observed at high resources. The rate of N_2O production significantly decreased and
244 ammonium production oscillated rather than steadily increased through time. These differences
245 in metabolite profiles clearly demonstrate that concentration influences the activities of pathway
246 bifurcation. Furthermore, repeated time series experiments that were extended up to 300 hours
247 show that nitrite is slowly depleted, but does not get fully consumed (Fig. S3). When cultures
248 were given nitrite, instead of nitrate as a terminal electron acceptor (8 mM lactate, 12 mM nitrite;
249 ratio=2), we observed no immediate growth (as was observed with nitrate) but measured more
250 N_2O than ammonium production (33.4±4.8 μmoles N_2O-N and 8.0±2.5 μmoles NH_4^+,
251 respectively) (Fig. S4), demonstrating respiratory ammonification does not exceed denitrification
252 when nitrite is supplied as the sole acceptor in *I. calvum*.

253 **Nitrite-reducing modules are up-regulated during late exponential- and stationary-phase**
254 **growth.** In order to gain insight into mechanisms of gene regulation and transcriptional
255 organization of *I. calvum*, we conducted RNA-Seq in parallel with the high resource time-series
256 metabolite profile. This approach enabled us to compare genome-wide differential expression
257 based on $\log_2$ fold change (lfc) of RNA extracted from three growth phases: early exponential
258 (EE), late exponential (LE), and stationary (ST) (Figs. 3B, S5). Within the central metabolic
259 pathway beginning with the conversion of lactate to pyruvate, we observed a moderate decrease

260 in transcript abundance of L-lactate dehydrogenase (LDH) (Intca_16740) between EE-LE and -
261 ST (lfc = -1.6±0.7; -1.9±0.7), respectively. Lactate utilization protein C (LUP) (Intca_04080), an
262 enzyme involved in lactate degradation, also showed a moderate and significant decrease in
263 transcript abundance between EE-LE and -ST (lfc = -1.6±0.6; -2.4±0.6, p=0.002), respectively. *I.*
264 *calvum* encodes for two parallel metabolic pathways for pyruvate conversion to acetyl-CoA:
265 pyruvate dehydrogenase (PDH) (Intca_01255) and pyruvate ferredoxin oxidoreductase (PFOR)
266 (Intca_15510). For PDH, there was a significant and moderate increase in transcript abundance
267 between EE-LE and -ST (lfc = 2.1±0.6, p=0.002; 1.5±0.6), respectively. For PFOR, there was a
268 minor decrease in transcript abundance between EE-LE (lfc = -0.43±0.5), and then a moderate
269 increase in transcript abundance between EE-ST (1.1±0.5). Citrate synthase (Intca_04135), the
270 enzyme catalyzing the conversion of acetyl-CoA to citrate and the first step of the tricarboxylic
271 acid (TCA) cycle, showed a highly significant increase in transcript abundance between EE-LE
272 and -ST (lfc = 4.3±0.5, p<0.001; 6.9±0.5, p<0.001). Within the ETC, there was moderate and
273 significant decrease in transcript abundance for all subunits from the primary dehydrogenase
274 (*nuo* complex; Intca_03465-03539) between EE-LE and -ST (lfc = -1.2±0.3; -2.4±0.6, p<0.001),
275 respectively. Nitrate reductase subunits showed no change in transcript abundance between EE-
276 LE (lfc = 0.01±0.07) and moderately decreased in abundance by ST (lfc = -1.2±0.1), which was
277 corroborated by the depletion of nitrate during stationary phase. There was a significant increase
278 in transcript abundance of *nirK* (Intca_17170) (lfc = 2.2±0.6, p=0.003; 2.4±0.6, p<0.001) and
279 quinol dehydrogenase/membrane anchor subunit *nrfH* (Intca_09465) (lfc = 2.5±0.6, p=0.001;
280 2.1±0.6, p=0.003) by EE-LT and EE-ST, respectively, which coincided with nitrite production
281 (Fig. 3A). The catalytic subunit of the cytochrome c nitrite reductase complex (*nrfA*)
282 (Intca_09460) also increased moderately in transcript abundance by EE-LT and EE-ST (lfc =
283 1.6±0.6; 1.0±0.6), respectively (Fig. 3B). Contrary to the transcript abundance patterns of *nirK*
284 and *nrfAH*, nitric oxide reductase (qNor; Intca_01525) transcripts moderately increased between
285 EE-LT (lfc = 1.6±0.6) but decreased in the successive time periods (lfc = 0.43±0.6 between EE-
286 ST; lfc = -1.2±0.6 between LE-ST) (Fig. 3B).

287 There was a significant increase in transcript abundance of formate transporter *focA*
288 (Intca_17150) between EE-ST, as well as LE-ST (lfc = 4.9±0.7, p=0.002; 4.8±0.7, p=0.002;
289 respectively). We verified the production of formate in our ion chromatography measurements in
290 the range of 100-200μM following late exponential growth. We also observed a moderate

291 increase in transcript abundance of formate dehydrogenase (FDH) subunits (Intca_11150-
292 11160). These results implicate the activity of formate oxidation, which would contribute to a Δp
293 in the periplasm via a Q-loop mechanism and the reduction of MK for electron transfer to nitrite
294 via cytochrome c nitrite reductase. Considering that formate was not provided in our media
295 recipe, an alternative pathway for formate production must exist in *I. calvum*. We also observed
296 acetate production in similar concentrations as formate (100-200μM). In *E. coli*, formate is
297 produced anaerobically from the action of pyruvate formate lyase (PFL). We identified a putative
298 PFL based on genome annotation (Intca_12230), where transcript abundance also significantly
299 increased by ST. PFL is also highly sensitive to oxygen (29), which was also in agreement with a
300 significant increase in transcript abundance between EE-ST and LE-ST (Fig. 3B) of cytochrome
301 *bd* oxidase (Intca_01110 and Intca_01115), which is thought to protect anaerobic enzymes
302 against oxidative stress (30).

303 **Discussion**

304 We challenge the paradigm that C:NO_3^- ratio strictly controls pathway selection in a dual-
305 pathway organism based on a simple principle: ratios do not account for the abundance of a
306 growth-limiting resource. We hypothesized that limitation in C or NO_3^- should better predict
307 pathway selection in a dual-pathway denitrifier/respiratory ammonifier. To test this hypothesis,
308 we systematically measured the response of the Gram-positive Actinobacterium
309 *Intrasporangium calvum* C5 to the same range of C:NO_3^- ratios at both high and low resource
310 loadings to better resolve mechanisms of pathway selection. We demonstrated that resource
311 concentration, not C:NO_3^- ratio, influences pathway selection. We found stronger support for
312 respiratory ammonification preference under C-limitation (at low C:NO_3^- ratios), which also
313 grew at significantly higher growth rates (Fig. 2). These results suggest that the NrfA complex,
314 which receives electrons directly from the MK-pool, is optimized to maximize power when one
315 or more resources are limiting. These data, together with metabolic reconstructions from
316 metabolite and transcriptional profiles (Fig. 3), suggest that C:NO_3^- ratio alone is insufficient to
317 explain pathway selection.

318 The theoretical basis for pathway selection is explained by the law of the minimum (LM) and the
319 maximum power principle (MPP), which state that growth is limited by the least abundant
320 resource and that biological systems are designed to maximize power in order to effectively

allocate energy to reproduction and survival (26), respectively. Here, it appears these two natural theories are working together: when resources are limited, the cell utilizes the respiratory pathway for growth that is optimized to maximize power. Power, in this case, is realized as higher growth rates from the cultures exhibiting disproportionately higher ammonium production than N_2O production (Fig. 2: high resources: $C:NO_3^-$ ratio = 0.1; low resources: $C:NO_3^-$ ratios = 4, 1, 0.5, 0.1; Fig. 3). More specifically, the bacterium must generate a greater Δp in order to maximize power when starved for a growth limiting resource. This may help to further explain how respiratory ammonification, which is overall energetically less favorable than denitrification (lactate with nitrite: ΔG^o = -763.98 versus ΔG^o = -1196.93, respectively), can have higher growth yields (25) and growth rates (Fig. 2, Fig. S1) under C- and N-limitation due to the higher energy yield on a per-nitrite basis (denitrification: -217 KJ per mole nitrite; respiratory ammonification: -399 KJ per mole nitrite). For comparison, a total of 8 H^+ are translocated during denitrification by *I. calvum* (not including nitrate reduction since both pathways share this step) (Fig. 3): NADH dehydrogenase translocates 4 H^+ per MKH_2 oxidized and the bc_1 complex translocates an additional 4 H^+ per MKH_2 oxidized. However, 2 H^+ must be consumed in the periplasm to reduce nitrite to NO (31). qNor has a net zero H^+ release (consumes 2 H^+ to make N_2O but releases 2 H^+) without MKH_2 regeneration (32). Thus, a net total of 6 H^+ are translocated per nitrite reduced in denitrification with added biosynthetic costs of making the bc_1 complex and qNor. In respiratory ammonification, MK/MKH_2 redox pair is cycled between NADH dehydrogenase and formate dehydrogenase. 6 electrons and 8 H^+ are needed to reduce nitrite to ammonium, thus 3 MKH_2 are needed (12). If MKH_2 is received from NADH dehydrogenase, 12 H^+ are translocated plus 2 H^+ from FDH. As each MKH_2 is oxidized at the binding site of NrfH, 2 H^+ are liberated (12), resulting in a net total of 12 H^+ translocated per nitrite reduced for respiratory ammonification. This implies that the cell might deplete its NADH pool more rapidly on a per nitrite basis. However, if more protons are pumped in the early stages of growth, the cell would be allocating the ATP generated for anabolism, as evidenced by higher growth rates in the cultures exhibiting higher amounts of respiratory ammonification (Fig. 2), which is supported by the MPP.

Following in the same line of reasoning for proton accounting in the ETC, *S. loihica* PV-4 (a Gram-negative dual-pathway γ-proteobacterium) and *I. calvum* use different types of nitrate reducing modules. *S. loihica* PV-4 utilizes NapA whereas *I. calvum* utilizes NarG (Fig. 1). The

352 latter translocates two H^+ per nitrate reduced while NapA consumes two H^+ in the periplasm
353 (13). Both reductases would generate a Δp via NADH dehydrogenase H^+ translocation, but the
354 NapA module would result in a net loss of two H^+, which may impact the selection of
355 downstream respiratory modules. For example, given the lower-than-expected observed growth
356 yields of denitrifiers compared to respiratory ammonifiers (25), if a NapA module is used, it
357 would make sense for respiratory ammonification to be selected under high C:N ratios because
358 the cell would need to compensate for less energy conservation during nitrate reduction. Nitric
359 oxide reductase composition may also impact pathway selection. For example, qNor does not
360 translocate H^+, while sNor, eNor, and gNor are predicted to conserve energy through H^+
361 translocation (32). Thus, the modularity of dissimilatory N reduction processes, and whether
362 those modules conserve energy or not, may impose certain constraints on pathway selection in
363 different organisms and should be further investigated as these considerations add significantly
364 to the biogeochemical tapestry of N-cycle dynamics and pathway evolution.

365 Under our high resource conditions (Fig. 2; left panels), at $C:NO_3^-$ ratios ≥ 1, we observed that
366 denitrification prevailed and these cultures had lower growth rates than the predominantly
367 ammonium producing cultures. These high resource circumstances resulted in the production of
368 toxic intermediates (i.e., NO_2^- and possibly NO, albeit at undetectable levels), which may explain
369 why these cultures had lower growth rates (Fig. 2; left panels) and quasi-steady state growth
370 curves in our high resource metabolite profile (Fig. 3A). Rowley and colleagues (33) reported
371 that at least 20% of the N_2O released during high resource conditions were produced by
372 competition between nitrite and nitrate in the active-site of NarG. Under excess C
373 concentrations, NarG produces intracellular NO from NO_2^- and these intermediates are likely
374 inhibitory to cell growth, which may explain why our growth curves (Fig. 3A) reached a quasi-
375 steady state before nitrate had been fully utilized (as compared to the low resource metabolite
376 profile, Fig. S2). Furthermore, resources were not limiting growth under these conditions.
377 Rather, the cells were likely experiencing toxicity from NO and NO_2^- and thus the metabolic
378 outcomes would be beyond the scope of the LM and MPP. Nonetheless, these results clearly
379 demonstrate that end-product formation from the two resource concentrations tested, with the
380 same $C:NO_3^-$ ratios, are not identical thereby refuting the $C:NO_3^-$ control hypothesis.

381 We selected a single treatment (8 mM lactate, 12 mM nitrate; C:NO_3^- ratio = 2), in which we
382 observed both denitrification and respiratory ammonification occurring simultaneously, for
383 RNA-Seq in order to gain insight into the transcriptional organization of actively growing *I.*
384 *calvum* cells. Strangely, we saw a decrease in transcript abundance encoding for two enzymes
385 known to convert lactate to pyruvate, LDH and LUP. While normalized read counts (Fig. S5)
386 were generally consistent across growth phases, indicative of constitutive expression, further
387 research investigating the mode of anaerobic lactate oxidation in *I. calvum* would illuminate how
388 reducing equivalents are fed into its central metabolic pathway. For example, *S. loihica* PV-4 is
389 known to use lactate for both denitrification and respiratory ammonification, but only uses
390 acetate for denitrification (20). Nonetheless, our transcriptomic data suggests that pyruvate plays
391 a central role in providing reducing equivalents to the TCA cycle as Acetyl-CoA, as evidenced
392 by significant upregulation in the genes encoding for PDH and citrate synthase, as well as
393 apparent "leaking" via incomplete lactate oxidation through the release of acetate and formate.
394 Such leaking may be produced by a putative PFL, adding to the diversity of C utilization
395 pathways feeding the ETC, and thereby driving pathway selection for nitrite reduction. Our
396 transcriptomic results, coupled with a parallel metabolite profile (Fig. 3A & 3B), also suggest
397 that the dual-pathway is induced by the presence of nitrite, and is not constitutively expressed
398 like nitrate reductase, *narG*. Furthermore, it appears that the significant increase in transcript
399 abundance for the gene encoding the *bd* oxidase helps to protect the anaerobic-dependent
400 biochemical machinery against oxidative stress, thereby scavenging any residual oxygen during
401 anaerobic growth. Undoubtedly, more conditions must be tested to better understand the
402 transcriptional organization of this unique bacterium.

403 Our metabolite profiles for N oxyanion respiration and N_2O versus ammonium production show
404 conflicting patterns relative to previous studies. Yoon and colleagues (21) reported complete
405 reduction of nitrate, production of nitrite, and then rapid consumption of nitrite, with N_2O as the
406 main end-product, by *S. loihica* PV-4 (5 mM lactate, 1 mM nitrate; ratio=0.6). When Yoon and
407 colleagues (21) replaced nitrate with nitrite as the dominant electron acceptor (5 mM lactate, 1
408 mM nitrite, ratio=0.6), ammonification prevailed. Other research has shown the same response to
409 nitrite replacement and ammonification dominance using non-fermentable C-sources (i.e.,
410 acetate) in chemostat enrichments of *Geobacter lovleyi* (34). In our work, nitrite was never fully
411 depleted (Figs. 3A, S1, S2) and when nitrite was given as the only electron acceptor, the

412 bacterium predominantly used denitrification but without concurrent growth (Fig. S4). Similar to
413 our work, Kraft and colleagues (22) also reported denitrification dominance when nitrite was
414 supplied as the terminal acceptor in incubations of coastal, sandy tidal flat sediments. These
415 differences highlight an incomplete understanding for the molecular mechanisms underlying the
416 framework put forth by the LM and MPP.

417 A detailed look into the biochemistry of ETC complexes helps to shed light on the molecular
418 mechanisms modulating pathway bifurcation. For example, Yoon and colleagues (3)
419 demonstrated that elevated pH selects for ammonification in *S. loihica* PV-4. This phenotypic
420 response is due to a decrease in the midpoint potential of the Rieske protein at higher pH (35–
421 37). Thus, any hindrance of electron flow through the bc_1 complex would ultimately reduce the
422 activity of downstream processes and promote alternative respiratory pathways. Nitrogen and C
423 limitation have also been shown to influence flux distributions in redox sensitive proteins,
424 including those found in electron transport (38). A drop in the intracellular redox potential (redox
425 poise) of the cell due to resource limitation may decrease the midpoint potential of the Rieske
426 protein and reduce the activity of any downstream electron exit modules, such as NirK (39–41).
427 Thus, based on fundamental principles of protein redox chemistry and thermodynamics, it
428 becomes clear that denitrification versus ammonification are likely not modulated by an arbitrary
429 ratio of $C:NO_3^-$, but rather by thermodynamic constraints of the Q-cycle (7, 8). The phenotypic
430 response of higher rates of denitrification over ammonification at high C:N ratios in other
431 published studies (3, 4) may also be due to enrichment bias for organisms that utilize quinones
432 with higher midpoint potentials in their bioenergetic chains (Fig. 1). Bergdoll and colleagues (7)
433 suggested that comparisons of Rieske/cyt*b* complexes from organisms with high- and low-
434 potential quinones may help to reconcile the thermodynamic properties of Q-cycle function.
435 However, most of our understanding of denitrification bioenergetics is based on evolutionarily
436 recent UQ-based HP bioenergetic chains from Gram-negative *α*-, *β*-, *γ*-proteobacteria. Because *I.*
437 *calvum* uses a MK-based LP bioenergetic chain it may be possible that the differences in
438 pathway selection across treatments are unique to LP chains.

439 Piecing together the evolutionary history of the N-cycle using isotopic signatures for
440 geochemically available N module cofactors (i.e., Ni, Fe, and Mo) coupled to molecular
441 evolutionary analysis has revealed respiratory ammonification was likely a major component of

442 the Archean N-cycle (28). Abiotic nitrite formation and depletion of ammonia through
443 photodissociation (42) would have created selective pressures for a dissimilatory N pathway that
444 also produced assimilatory N. We demonstrate that NrfA proteins are significantly enriched in N
445 compared to NirK (i.e., no evolutionary constraints to cost minimize N in the *nrfA* gene product
446 (11)) (Fig. 1B) and that ammonium production (without accumulation in the medium) supports
447 growth in *I. calvum* (Fig. 1C). The Nrf module is also relatively simplistic in that it receives
448 electrons directly from the quinol pool and not the bc_1 complex used in denitrification. The early
449 exit of electrons from the ETC (i.e., before reaching the bc_1 complex) suggests that Nrf may have
450 originated prior to the bc_1 complex. Furthermore, the quinol oxidation site (Q_o) of cytochrome *b*
451 contains a PDWY motif, indicative of an ancestral LP respiratory chain found in many Gram-
452 positive organisms (43). However, there is still debate regarding the presence of a cytochrome *bc*
453 complex in the last universal common ancestor (LUCA) (43, 44). Lastly, the Nrf module is wired
454 to operate via a q-loop with formate dehydrogenase whose Mo-cofactors would have also been
455 bioavailable during the Archean, further supporting an early evolution.

456 In summary, we employ a new predictive framework that accounts for the biochemistry and
457 evolutionary history of N modules, ETC complexes, and pool quinones to suggest the
458 mechanisms by which these two pathways are regulated at the molecular level. With this
459 understanding, it may be possible to extend our framework to environmental microbial
460 populations and accelerate model development across different ecosystem scales (i.e., cross-scale
461 systems biology).

462 **Materials and Methods**

463 **Culture Conditions**

464 Sample collection: *I. calvum* was isolated from a groundwater well (GW247) collected on
465 2/18/2013 at Oak Ridge National Laboratory (Lat: 35.97990, Long: 84.27059) with a
466 groundwater temperature of 15.57 ºC, conductivity of 521.9 µS/cm, and pH of 7.71. *I. calvum*
467 was isolated and obtained from Dr. R. Chakraborty (Lawrence Berkeley National Laboratory).
468 We began our experimental process by first picking single colonies from LB agar plates and
469 transferring the clonal isolates to LB broth.

470 Media preparation: All subsequent cultures were grown at 30 ºC and shaken at 250 rpm. Nitrate
471 reducing minimal media was prepared with the following final concentrations: NaCl (0.6mM),
472 NH_4Cl (1.75mM) (for ammonium replete conditions but not used in NH4-deplete conditions),
473 MgCl2 (0.2mM), CaCl2 (0.04mM), KCl (0.1mM), K2HPO4 (0.01mM), NaHCO3- (0.3mM),
474 cysteine (1mM) as reducing agent, resazurin as redox indicator, and trace elements and trace
475 vitamin solutions as reported (20, 45). 1M sterile filtered (0.2µm) Concentrated stocks of 60%
476 w/w sodium DL-lactate solution (Sigma-Aldrich, St. Louis, MO, USA), sodium-nitrate and
477 sodium-nitrite (≥99%, Fisher Scientific, Pittsburg, PA, USA) were diluted into media prior to
478 autoclaving to achieve the desired C:NO_3^- ratio. C:NO_3^- ratio was calculated based on (3) where
479 the number of C atoms (n) in the e-donor is multiplied by the concentration of the e-donor,
480 divided by the number of N atoms in the e-acceptor multiplied by the concentration of the e-
481 acceptor (Table S1). Media preparation was conducted in a 2L Widdel Flask. After autoclaving,
482 the media was immediately put under an anoxic headspace (N2/CO2 80:20 mix) and sterile
483 filtered (0.2µm) trace elements, trace vitamins, and reducing agent were added. The media was
484 cooled under an anoxic headspace and buffered with bicarbonate to maintain a pH of 7.2.
485 Hungate technique was used to dispense media into culture tubes (20 mL) and serum vials (100
486 mL) pre-flushed with a sterile stream of ultra-high purity (UHP) N_2 and sealed with blue 1" butyl
487 rubber stoppers. End-point cultures were grown in Balch tubes (18x150-mm glass tube) sealed
488 with butyl rubber stoppers. Cultures for time-course sampling were grown in 160ml serum vials.
489 All end-point experiments were terminated after 100 hours unless otherwise noted. Mean pH for
490 all culture vessels (time series and end-point; Table S5), measured at the end of each experiment,
491 was 7.3±0.05 (n=144)

492 **Analytical procedures**

493 Growth Curve/Cell counts/Yield Measurements: Growth curves were measured from scratch-
494 free Balch-tubes grown cultures using an automated optical density reader at OD_{600} nm
495 (Lumenautix LLC, Reno, NV). End-point cultures were monitored until all replicates reached
496 stationary phase (65-100 hours depending on C:NO_3^- treatment) (Fig. S6).

497 Cell counts were performed by fixing cells in 4% paraformaldehyde (final concentration) for 20
498 minutes, filtered onto 0.2µm pore-sized black polycarbonate filters, and washed three times with
499 phosphate buffered saline (PBS, pH 7.2). Filtered cells captured on the black polycarbonate

500 filters were stained with SYBR® Gold nucleic acid stain (10-minute incubation) (ThermoFisher
501 Scientific) and counted manually with a fluorescence microscope (Olympus BX60, Tokyo,
502 Japan). We collected cells from during lag phase, exponential phase, and stationary phase in
503 order to create a standard curve of cell counts versus optical density (OD_{600}). We fit a linear
504 model to cell count versus OD_{600} (R^2=0.99) and used the resulting linear equation for cell count
505 enumeration for growth curves during our various treatment conditions.

506 Biomass concentrations were measured by filtration and drying as per standard protocol (46) for
507 8mM lactate/12mM nitrate and 0.8mM lactate/1.2mM nitrate treatments and conducted in
508 parallel with growth curve/cell counts as described above. Analysis from triplicate cultures
509 yielded (0.064 ± 0.003) and (0.016 ± 0.001) mg of biomass (dry weight) ml^{-1} for 8mM and 0.8
510 mM lactate cultures, respectively. Cell counts from stationary phase cultures were (1.5 ± 0.05) x
511 10^7 and (1.16 ± 0.09) x 10^6 for 8mM and 0.8 mM lactate cultures, respectively. From these
512 values the dry weight of a single *I. calvum* cell was estimated to be 1.09 x 10^{-10} g. Growth yield
513 (*Y*) (Table S4) was calculated by dividing biomass (g) by lactate mass (g) and moles consumed,
514 as described by (47). Lactate measurements are described below.

515 Ion and Gas Chromatography Measurements: A dual channel Dionex ICS-5000+ (Thermo
516 Scientific) was used to measure all anions (AS11-HC) and cations (CS-16) from the bacterial
517 growth media. New glass IC vials were used for every sample in order to ensure no cross
518 contamination of analytes. Headspace gas from Balch tubes and serum vials was sampled with
519 volume appropriate gastight syringes (Hamilton Company, Reno, NV) pre-flushed with UHP N_2.
520 For high and low resource treatments, 10µl and 100µl of headspace were sampled and diluted
521 into 12ml exetainters (Labco, Lampter, Wales, UK) over-pressurized with 15ml UHP N_2,
522 respectively. Similar dilutions were performed for nitrite as e-acceptor experiments, ammonium-
523 deplete experiments, and time-series experiments. For time-series experiments, an equal volume
524 of headspace gas that was removed at each time-point was replaced with sterile UHP N_2. N_2O
525 was measured by gas chromatography (Shimadzu Greenhouse Gas Analyzer GC-2014) using a
526 500µl injection volume. The rubber septa on the injection port of the GC was replaced after 100
527 injections in order to prevent leakage of the sample after the injection needle was lifted out from
528 the injection port. Aqueous concentrations of N_2O were calculated using a Henry's constant of

529 1.751 (mM (g)/mM (aq)) corrected for the medium's ionic strength and temperature. A total of
530 8-11 replicates per treatment were analyzed for all experiments discussed in this work.

531 Ammonium production calculations:

532 All nitrogen needed for assimilation must be first converted into ammonium (47). This fact
533 makes ammonium production measurements via respiratory nitrite ammonification difficult since
534 the cells simultaneous consume ammonium for growth. Therefore, direct measurements of
535 ammonium from IC or spectrophotometric analyses would not yield accurate production values.
536 Because *I. calvum* simultaneously consumes ammonium as its sole N source for growth and
537 produces ammonium via respiratory nitrite ammonification, we first measured ammonium
538 consumption with O_2 and lactate by calculating the difference between starting and ending
539 ammonium concentrations. These ammonium consumption values were then normalized to
540 lactate consumed (0.31μmols NH_4^+/lactate) and to ammonium consumed per cell, which was
541 calculated from average cell number of stationary phase biomass (Fig. S7) (7.07×10^{-7}μmols
542 NH_4^+/cell). These two ammonium consumption constants were used as two separate methods to
543 compare ammonium production based on actual starting and ending ammonium/lactate
544 measurements and cell number during nitrate reducing minimal media experiments.

545 For ammonium production normalized to lactate consumption, calculations are based on a mass
546 balance approach from (48) for Total Belowground Carbon Allocation (TBCA) but adapted for
547 nitrogen flux instead of carbon flux:

548 $$\text{Net } NH_4^+{}_{(APL)} = (\Delta\text{lactate}_{\text{start-end}} \times 0.31\mu\text{mols } NH_4^+/\text{lactate}) + \Delta NH_4^+{}_{\text{end-start}}$$

549 Here, the $\Delta\text{lactate}_{\text{start-end}}$ variable (μmols) is multiplied by the ammonium consumed per lactate
550 consumed constant (APL). This value is added to the $\Delta NH_4^+{}_{\text{end-start}}$ variable (μmols), denoted as
551 ending minus starting concentration, which defines whether the change in ammonium is positive
552 (more ammonium produced than consumed) or negative (more ammonium consumed than
553 produced). The ammonium production method using cell count (APC) is calculated as reported
554 by (20), where :

555 $$\text{Net } NH_4^+{}_{(APC)} = (\text{Cell Yield} \times 7.07 \times 10^{-7}\mu\text{mols } NH_4^+/\text{cell}) + \Delta NH_4^+{}_{\text{end-start}}$$

556 Where Cell Yield is the number of cells at stationary phase (Fig. S6). Comparison of these two
557 ammonia production methods revealed that they are in agreement with each other for anaerobic
558 nitrate reducing media experiments (Fig. S8). However, because the cell counts under low
559 resource treatments were at the lower limit of our standard curve (OD versus cell count), we
560 observed slightly more variability using the APC method. Lactate measurements by IC gave us
561 higher sensitivity over the large range of treatments tested, thus we report the APL method in the
562 main text as the preferred method for reporting ammonium production by respiratory
563 ammonification.

564 **Nucleic Acid Extraction and Sequencing**

565 DNA for genome sequencing was extracted with phenol-chloroform. The DNA quality and
566 integrity was verified on Agilent 2200 TapeStation and DNA was sequenced on the PacBio
567 platform (Duke Center for Genomic and Computational Biology).

568 For gene expression analysis, *I. calvum* cells were grown in 300 mL batch cultures under 8mM
569 and 0.8mM lactate (12mM and 1.2mM nitrate, respectively) (n=3). Growth curves were
570 monitored in real-time to collect cells during early-exponential, late-exponential, and stationary
571 phase. Upon sampling, culturing vessels were immediately incubated on ice, aseptically
572 transferred to 50 mL falcon tubes and immediately centrifuged at 15000 G for 5 minutes at 4 ºC.
573 Supernatant was immediately poured off and the cell pellets were harvested and stored in TRIzol
574 Reagent (Ambion RNA by Life Technologies) at -80 ºC until further processing. RNA was
575 extracted with TRIzol Reagent (Ambion RNA by Life Technologies), following the
576 manufacturer's protocol. The extraction was scaled up to 20 ml of TRIzol and performed in 50
577 ml conical tubes. RNA was resuspended in water, treated with Baseline-ZERO DNase
578 (Epicentre) and cleaned up with RNeasy MinElute Cleanup Kit (QIAGEN). Total extracted RNA
579 from each growth phase was quantified (RiboGreen RNA quantification), analyzed for RNA
580 integrity number (RIN) (RIN≥0.8 were used for sequencing), treated with RiboZero rRNA
581 removal kit (Illumina, San Diego, CA). Library preparation was performed with the TruSeq
582 Stranded mRNA Library Prep kit (Illumina, San Diego, CA) and sequenced using Illumina
583 NextSeq 500 2x150 Mid Output v2 platform, resulting in 10-15 million reads per sample.

584

585 **Phylogenetic, Genomic, and Transcriptomic Analysis**

586 Genomic DNA was assembled using Canu with an estimated genome size of 5 million base pairs
587 (49). The resulting single contiguous fragment was aligned to the *I.* calvum 7KIP genome (Acc:
588 NC_014830.1) to compare sequence similarity in Mauve (50, 51). Genome annotation for C5
589 was performed by the DOE Joint Genome Institute (JGI) using the Isolate Genome Gene Calling
590 method (Prodigal V2.6.3 February, 2016) under the submission ID 172966. The complete
591 genome sequence is deposited into NCBI BioProject SUB4141755.

592 A set of 34 NrfA amino acid sequences, representing 33 complete genome sequences and 1
593 octaheme nitrite reductase (ONR) from known respiratory ammonification organisms were
594 downloaded from GenBank (Table S1). A multiple sequence alignment (MSA) was generated
595 from the sequences annotated as cytochrome c nitrite reductase and ONR using MUSCLE (52).
596 The resulting alignment was visualized within MEGA5 (53) where the alignment was manually
597 screened for the presence of conserved amino acid residues consistent with those found in NrfA
598 (i.e., heme motifs). A maximum likelihood tree was created from the alignment using RAxML
599 (54) with 500 bootstrap iterations. The presence of NapA, NarG, NirK, and Nor modules were
600 manually queried from each NCBI genome in our set and confirmed by MSA, as described
601 above. Metabolic pathway for pool quinone type was queried on BioCyc Pathway/Genome
602 Database (biocyc.org) for each organism in our set. The structure of *I. calvum*'s NirK protein
603 was predicted using the protein structure predicting algorithm Phyre2 (55). Protein atomic
604 composition for C and N was calculated from amino acid sequences as input files, as described
605 by (10, 11), using custom python scripts for each element separately
606 (github.com/dvuono/Cost_minimization).

607 For transcriptomic analysis, the resulting raw reads were inspected using FastQC (56) to
608 determine quality, read length, and ambiguous read percentage. Reads were trimmed based on
609 quality score with a sliding window of 5 base pairs, quality cutoff of 28, trailing cutoff quality
610 score of 10, as well as adapter contamination removal in Trimmomatic (57). Due to the high
611 similarity of C5 to 7KIP, reads were aligned to the *Intrasporangium calvum* genomic reference
612 sequence and gtf file (Acc: NC_014830.1) using the STAR RNA-seq aligner (58), with the --
613 limitBAMsortRam parameter set to the recommended value by STAR. Sequence reads were
614 mapped to genomic features to obtain count data using featureCounts (59). Systematic changes

across experimental conditions were performed on normalized read counts in DESeq2 (60). The RNA-seq data reported in this study have been deposited in NCBI BioProject SUB4141755.

Statistical analyses were conducted in the R environment for statistical computing (r-project.org). Data that was tested using parametric statistical analysis were first validated for normality by visualizing the data as a histogram and testing via Shapiro-Wilks test for normality.

ACKNOWLEDGMENTS. We thank F. von Netzer, K. Hunt, S Morales, N. Stopnisek, K. Meinhardt, W. Qin, N Elliot, T. Hazen, H. Carlson, B. Ramsey, A. Murray, Z. Harrold, T. Morgan, P. Longley, and R. Hallnan. This research was supported by a grant from the Nevada Governor's office of Economic Development (JG), by the Desert Research Institute (DRI) postdoctoral research fellowship program, and in part by Ecosystems and Networks Integrated with Genes and Molecular Assemblies (ENIGMA) (http://enigma.lbl.gov)—a Scientific Focus Area Program at Lawrence Berkeley National Laboratory under contract number DE-AC02-05CH11231 and funded in part by Oak Ridge National Laboratory under contract DE-AC05-00OR22725, and is based upon work supported by the U.S. Department of Energy, Office of Science, Office of Biological & Environmental Research.

1. Galloway JN, et al. (2003) The Nitrogen Cascade. *Bioscience* 53(4):341.

2. Tiedje JM, Sexstone AJ, Myrold DD, Robinson JA (1982) Denitrification: ecological niches , competition and survival. *Antonie Van Leeuwenhoek* 48(10598):569–583.

3. Yoon S, Cruz-García C, Sanford R, Ritalahti KM, Löffler FE (2015) Denitrification versus respiratory ammonification: Environmental controls of two competing dissimilatory NO 3-/NO 2-reduction pathways in Shewanella loihica strain PV-4. *ISME J* 9(5):1093–1104.

4. van den Berg EM, van Dongen U, Abbas B, van Loosdrecht MC (2015) Enrichment of DNRA bacteria in a continuous culture. *ISME J* 9(10):2153–2161.

5. Moparthi VK, Hägerhäll C (2011) The evolution of respiratory chain complex i from a smaller last common ancestor consisting of 11 protein subunits. *J Mol Evol* 72(5–6):484–497.

6. Dibrova D V., Cherepanov DA, Galperin MY, Skulachev VP, Mulkidjanian AY (2013) Evolution of cytochrome bc complexes: From membrane-anchored dehydrogenases of ancient bacteria to triggers of apoptosis in vertebrates. *Biochim Biophys Acta - Bioenerg* 1827(11–12):1407–1427.

7. Bergdoll L, Ten Brink F, Nitschke W, Picot D, Baymann F (2016) From low- to high-potential bioenergetic chains: Thermodynamic constraints of Q-cycle function. *Biochim Biophys Acta* 1857(9):1569–1579.

8. Schoepp-Cothenet B, et al. (2009) Menaquinone as pool quinone in a purple bacterium. *Proc Natl Acad Sci* 106(21):8549–54.

9. Soo RM, Hemp J, Parks DH, Fischer WW, Hugenholtz P (2017) On the origins of oxygenic photosynthesis and aerobic respiration in Cyanobacteria. *Science (80-)* 355(6332):1436–1440.

10. Baudouin-Cornu P, Schuerer K, Marlière P, Thomas D (2004) Intimate evolution of proteins: Proteome atomic content correlates with genome base composition. *J Biol Chem* 279(7):5421–5428.

11. Grzymski JJ, Dussaq AM (2012) The significance of nitrogen cost minimization in proteomes of marine microorganisms. *ISME J* 6(1):71–80.

12. Einsle O, Messerschmidt A, Huber R, Kroneck PMH, Neese F (2002) Mechanism of the six-electron reduction of nitrite to ammonia by cytochrome c nitrite reductase. *J Am Chem Soc* 124(39):11737–11745.

13. Kraft B, Strous M, Tegetmeyer HE (2011) Microbial nitrate respiration - Genes, enzymes and environmental distribution. *J Biotechnol* 155(1):104–117.

14. Godfrey L V., Falkowski PG (2009) The cycling and redox state of nitrogen in the Archaean ocean. *Nat Geosci* 2(10):725–729.

15. Nitschke W, Dracheva S (1995) Reaction center associated cytochromes in Anoxygenic Photosynthetic Bactera. eds Blankenship R, Madigan M, Bauer C (Kluwer Academic, Dordrecht, The Netherlands), pp 775–805.

16. Lalucat J, Bennasar A, Bosch R, Garcia-Valdes E, Palleroni NJ (2006) Biology of Pseudomonas stutzeri. *Microbiol Mol Biol Rev* 70(2):510–547.

17. Suharti, de Vries S (2005) Membrane-bound denitrification in the Gram-positive bacterium Bacillus azotoformans. *Biochem Soc Trans* 33(Pt 1):130–133.

18. Heylen K, Keltjens J, Stein LY (2012) Redundancy and modularity in membrane-associated dissimilatory nitrate reduction in Bacillus. *Front Microbiol* 3(371):1–27.

19. Decleyre H, Heylen K, Bjorn T, Willems A (2016) Highly diverse nirK genes comprise two major clades that harbour ammonium-producing denitrifiers. *BMC Genomics* 17(1):1–13.

20. Yoon S, Sanford RA, Löffler FE (2013) Shewanella spp. Use acetate as an electron donor for denitrification but not ferric iron or fumarate reduction. *Appl Environ Microbiol* 79(8):2818–2822.

21. Yoon S, Sanford RA, Löffler FE (2015) Nitrite control over dissimilatory nitrate/nitrite reduction pathways in Shewanella loihica strain PV-4. *Appl Environ Microbiol* 81(10):3510–3517.

22. Kraft B, et al. (2014) The environmental controls that govern the end product of bacterial nitrate respiration. *Science (80-)* 345(6197):676–679.

23. Schmidt CS, Richardson DJ, Baggs EM (2011) Constraining the conditions conducive to dissimilatory nitrate reduction to ammonium in temperate arable soils. *Soil Biol Biochem* 43(7):1607–1611.

24. Hardison AK, Algar CK, Giblin AE, Rich JJ (2015) Influence of organic carbon and nitrate loading on partitioning between dissimilatory nitrate reduction to ammonium (DNRA) and N<inf>2</inf> production. *Geochim Cosmochim Acta* 164:146–160.

25. Strohm TO, Griffin B, Zumft WG, Schink B (2007) Growth yields in bacterial denitrification and nitrate ammonification. *Appl Environ Microbiol* 73(5):1420–1424.

26. Lotka AJ (1922) Contribution to the Energetics of Evolution. *Proc Natl Acad Sci* 8(6):147–151.

27. Kalakoutskii LV, Kirillova IP, Krassilnikov NA (1967) a New Genus of the. *J Gen Microbiol* 48:373-79–85.

28. Klotz MG, Stein LY (2008) Nitrifier genomics and evolution of the nitrogen cycle. *FEMS Microbiol Lett* 278:146–156.

29. Abbe KS, Takahashi S, Yamada T (1982) Invovlement of oxygen-sensitive pyruvate-formate lysase in mixed-acid fermetnation by Streptococcus mutans under strictly anerobic conditions. *J Bacteriol* 152(1):175.

30. Das A, Silaghi-Dumitrescu R, Ljungdahl LG, Kurtz DM (2005) Cytochrome *bd* oxidase, oxidative stress, and dioxygen tolerance of the strictly anaerobic bacterium *Moorella thermoacetica*. *J Bacteriol* 187(6):2020–2029.

691 31. Zumft WG (1997) Cell biology and molecular basis of denitrification. *Microbiol Mol Biol Rev* 61(4):533–
692 616.

693 32. Hemp J, Gennis RB (2008) Diversity of the Heme-Copper Superfamily in Archaea: Insights from Genomics
694 and Structural Modeling. *Results and Problems in Cell Differentiation*, eds Schäfer G, Penefsky HS
695 (Springer Science+Business Media), pp 1–28.

696 33. Rowley G, et al. (2012) Resolving the contributions of the membrane-bound and periplasmic nitrate
697 reductase systems to nitric oxide and nitrous oxide production in Salmonella enterica serovar Typhimurium.
698 *Biochem J* 762:755–762.

699 34. van den Berg EM, Rombouts JL, Kuenen JG, Kleerebezem R, van Loosdrecht MCM (2017) Role of nitrite
700 in the competition between denitrification and DNRA in a chemostat enrichment culture. *AMB Express*
701 7(91):1–7.

702 35. Link TA, Hagen WR, Pierik AJ, Assmann C, von Jagow G (1992) Determination of the redox properties of
703 the Rieske cluster of bovine heart bc1 complex by direct electrochemistry of a water- soluble fragment.
704 *EurJBiochem* 208:685–691.

705 36. Ugulava NB, Crofts AR (1998) CD-monitored redox titration of the Rieske Fe-S protein of Rhodobacter
706 sphaeroides: pH dependence of the midpoint potential in isolated bc1 complex and in membranes. *FEBS*
707 *Lett* 440(3):409–413.

708 37. Zu Y, et al. (2003) Reduction Potentials of Rieske Clusters: Importance of the Coupling between Oxidation
709 State and Histidine Protonation State. *Biochemistry* 42:12400–12408.

710 38. Ansong C, et al. (2014) Protein redox dynamics during light-to-dark transitions in cyanobacteria and
711 impacts due to resource limitation. *Front Microbiol* 5(July):1–10.

712 39. Snyder CH, Merbitz-Zahradnik T, Link TA, Trumpower BL (1999) Role of the Rieske Iron – Sulfur Protein
713 Midpoint Potential in the Protonmotive Q-Cycle Mechanism of the Cytochrome bc 1 Complex. *J Bioenerg*
714 *Biomembr* 31(3):235–242.

715 40. Denke E, et al. (1998) Alteration of the midpoint potential and catalytic activity of the Rieske iron-sulfur
716 protein by changes of amino acids forming hydrogen bonds to the iron-sulfur cluster. *J Biol Chem*
717 273(15):9085–9093.

718 41. Hunte C, Solmaz S, Palsdóttir H, Wenz T (2008) A structural perspective on mechanism and function of the
719 cytochrome bc1 complex. *Results and Problems in Cell Differentiation*, eds Schäfer G, Penefsky HS
720 (Springer Science+Business Media), pp 253–270.

721 42. Falkowski PG (1997) Evolution of the nitrogen cycle and its influence on the biological sequestration of
722 CO2 in the ocean. *Nature* 387(6630):272–275.

723 43. Kao WC, Hunte C (2014) The molecular evolution of the Qo Motif. *Genome Biol Evol* 6(7):1894–1910.

724 44. Dibrova D V., Cherepanov DA, Galperin MY, Skulachev VP, Mulkidjanian AY (2013) Evolution of
725 cytochrome bc complexes: From membrane-anchored dehydrogenases of ancient bacteria to triggers of
726 apoptosis in vertebrates. *Biochim Biophys Acta - Bioenerg* 1827(11–12):1407–1427.

727 45. Hillesland KL, et al. (2014) Erosion of functional independence early in the evolution of a microbial
728 mutualism. *Proc Natl Acad Sci* 111(41):14822–14827.

729 46. APHA (2012) *Standard Methods for the Examination of Water and Wastewater* (American Public Health
730 Association: Washington, DC). 23rd Ed. doi:ISBN 9780875532356.

731 47. White D (2000) *The physiology and biochemistry of prokaryotes* (Oxford University Press). 3rd ed.

732 48. Giardina CP, Ryan MG (2002) Total belowground carbon allocation in a fast-growing Eucalyptus plantation
733 estimated using a carbon balance approach. *Ecosystems* 5(5):487–499.

734 49. Koren S, et al. (2017) Canu : scalable and accurate long- - - read assembly via adaptive k - - - mer weighting
735 and repeat separation. *Genome Res*:1–35.

736 50. Darling ACE, Mau B, Blattner FR, Perna NT (2004) Mauve : Multiple Alignment of Conserved Genomic
737 Sequence With Rearrangements. *Genome Res* 14:1394–1403.

738 51. Darling AE, Mau B, Perna NT (2010) Progressivemauve: Multiple genome alignment with gene gain, loss
739 and rearrangement. *PLoS One* 5(6):e11147.

740 52. Edgar RC (2004) MUSCLE: multiple sequence alignment with high accuracy and high throughput. *Nucleic*
741 *Acids Res* 32(5):1792–7.

742 53. Tamura K, et al. (2011) MEGA5: Molecular evolutionary genetics analysis using maximum likelihood,
743 evolutionary distance, and maximum parsimony methods. *Mol Biol Evol* 28(10):2731–2739.

744 54. Stamatakis A (2014) RAxML version 8: A tool for phylogenetic analysis and post-analysis of large
745 phylogenies. *Bioinformatics* 30(9):1312–1313.

746 55. Kelley LA, Mezulis S, Yates C, Wass M, Sternberg M (2015) The Phyre2 web portal for protein modelling,
747 prediction, and analysis. *Nat Protoc* 10(6):845–858.

748 56. Andrews S (2010) FastQC: A quality control tool for high throughput sequence data. *Available online at:*
749 *http:// www.bioinformatics.babraham.ac.uk/projects/fastqc*.

750 57. Bolger AM, Lohse M, Usadel B (2014) Trimmomatic: A flexible trimmer for Illumina sequence data.
751 *Bioinformatics* 30(15):2114–2120.

752 58. Dobin A, et al. (2013) STAR: Ultrafast universal RNA-seq aligner. *Bioinformatics* 29(1):15–21.

753 59. Liao Y, Smyth GK, Shi W (2014) FeatureCounts: An efficient general purpose program for assigning
754 sequence reads to genomic features. *Bioinformatics* 30(7):923–930.

755 60. Love MI, Huber W, Anders S (2014) Moderated estimation of fold change and dispersion for RNA-seq data
756 with DESeq2. *Genome Biol* 15(12):1–21.

757

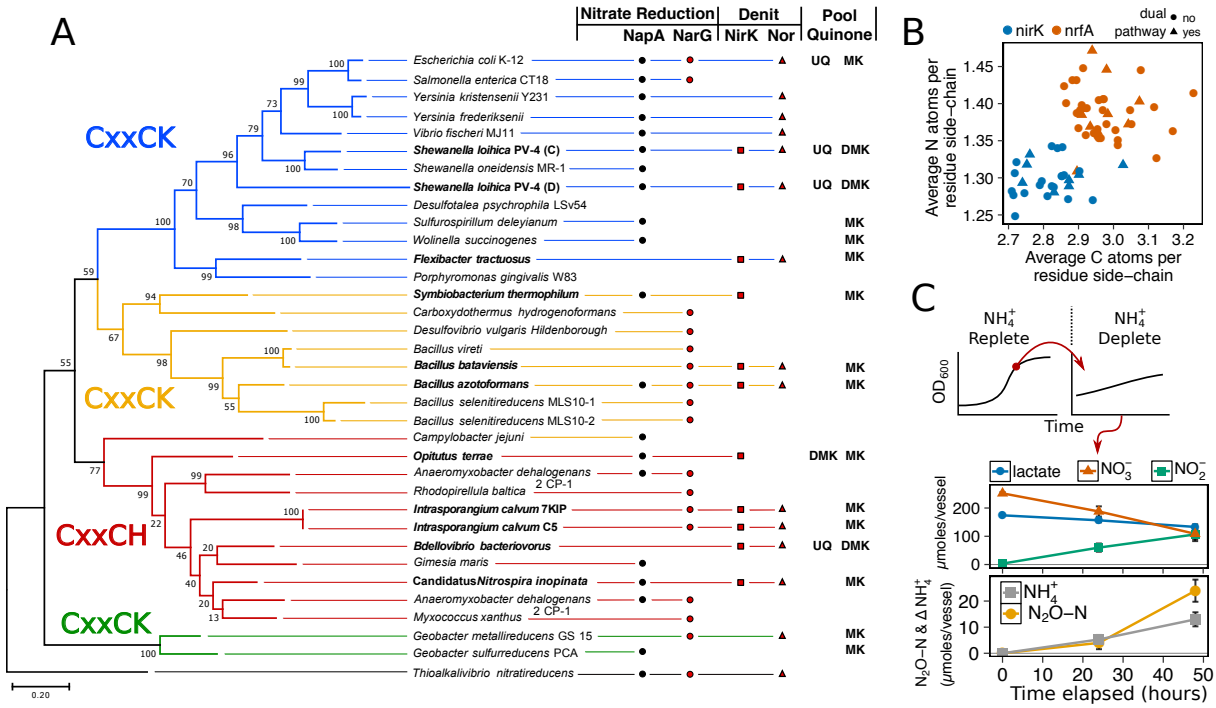

Figure 1. (A) Maximum likelihood phylogenetic tree of NrfA amino acid sequences from known respiratory ammonifiers and accompanying N-module composition for each organism. Pool quinone is also noted for dual-pathway nitrite reducers and model species. Colors of the main branches denote the 1st heme motif type: CxxCK and CxxCH. (B) Protein atomic composition for N and C normalized to protein length for NirK and NrfA nitrite reductases. (C) State-transition from ammonium-replete to ammonium-deplete for *I. calvum* C5 grown under 8mM lactate 12mM nitrate minimal media at 30 ºC. Metabolite profiles for ammonium-deplete are shown.

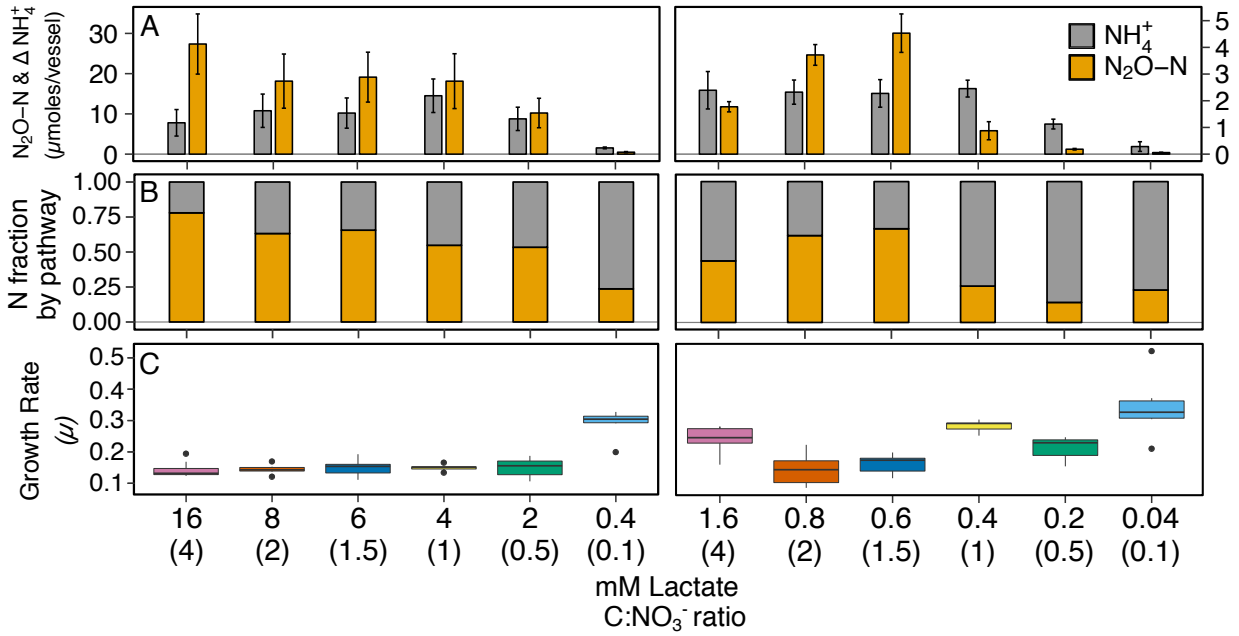

Figure 2. The effects of high resource (left; range of lactate concentrations with 12 mM NO_3^-) and low resource (right; range of lactate concentrations with 1.2 mM NO_3^-) concentrations with the same C:NO_3^- ratio on pathway selection in *I. calvum* C5. (A) Production of N_2O-N and net change of NH_4^+ over a 100-hour incubation period at 30 ºC. Each bar represents the average of 8-10 replicates per treatment (Table S5). (B) Fraction of dissimilated N by pathway. (C) Growth rates for each corresponding treatment. The x-axis label defines lactate concentration and C:NO_3^- ratio in parentheses.

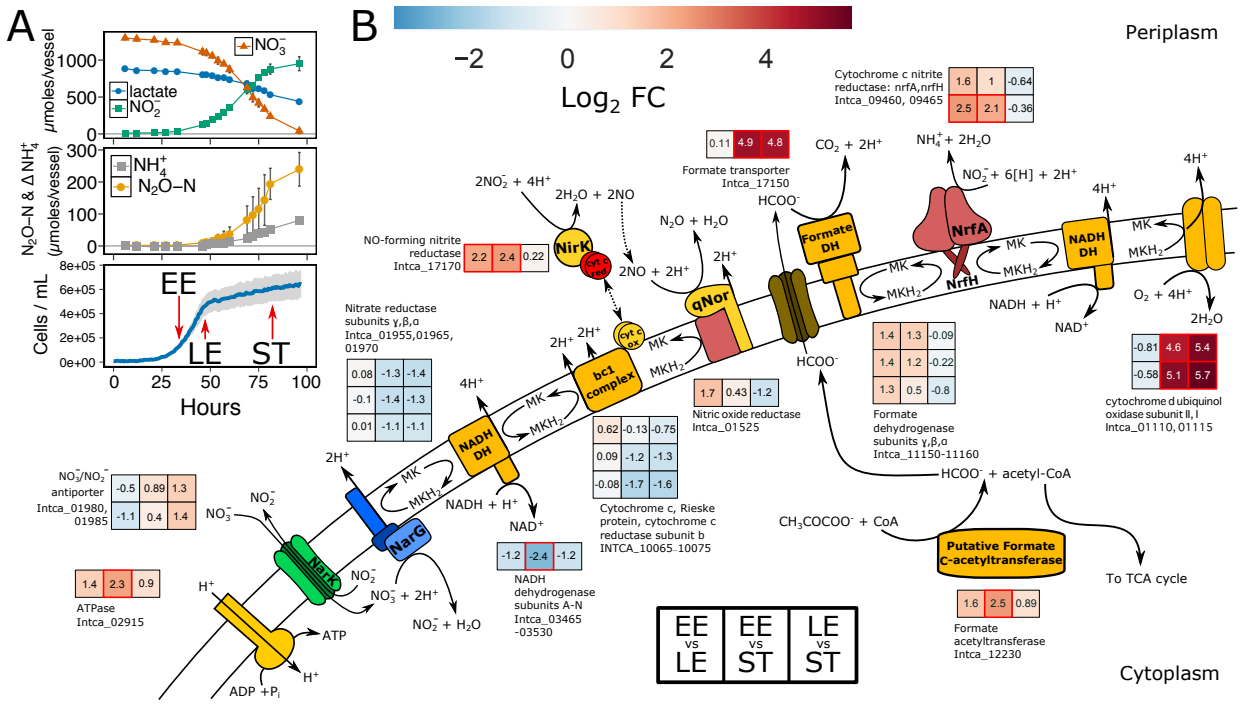

Figure 3. (A) Time-series metabolite profiles for lactate, nitrate, and nitrite (top pane), production of dissimilated end-products as N_2O-N and net change in NH_4^+ ammonium production (middle pane), and corresponding growth curve of *I. calvum* cells grown under 8mM lactate 12mM nitrate (C:NO_3^- ratio = 2) (bottom pane). Sampling points during growth phases are marked for transcriptomic analysis. (B) Metabolic reconstruction of the ETC from *I. calvum* with transcriptional changes for genes participating in dual-pathway dissimilatory nitrite reduction. Log_2 fold changes in transcript abundance are shown for late exponential relative to early exponential growth phase (EE vs. LE), stationary phase relative to early exponential growth phase (EE vs. ST), and stationary phase relative to late exponential growth phase (LE vs. ST). Locus IDs for each gene product correspond to heat map subplots in the order shown (left-to-right for each growth phase and top-to-bottom for each locus ID specified). Higher transcript abundance is represented in red, lower transcript abundance in blue, and no change in transcript abundance in white. Significant changes in transcript abundance ($p < 0.01$) are marked as a red box. Value of log_2 fold change is specified within each subplot. The log_2 fold changes of 14 NADH dehydrogenase subunits (Intca_03465-03530) were averaged as transcriptional changes were all shifted in the same direction.